The Astrophysical Journal Letters, 995:L45 (12pp), 2025 December 20 https://doi.org/10.3847/2041-8213/ae24e2

A Sudden Fine-scale Bright Kernel Captured by Hi-C Flare in 11 MK Emission during an M1.6-class Solar Flare's Postmaximum Phase

Sanjiv K. Tiwari[1,2], Navdeep K. Panesar[1,3], Ronald L. Moore[4,5], Sabrina L. Savage[4], Amy R. Winebarger[4], Genevieve D. Vigil[4], Juraj Lörinčík[1,2], Vanessa Polito[1], Bart De Pontieu[1,6,7], Leon Golub[8], Ken Kobayashi[4], Patrick Champey[4], Jenna Samra[8], Anna Rankin[9], Robert W. Walsh[9], Crisel Suarez[8,10], Christopher S. Moore[8], Adam R. Kobelski[4], Jeffrey W. Reep[11], and Charles Kankelborg[12]
[1] Lockheed Martin Solar and Astrophysics Laboratory, 3251 Hanover St., Bldg. 203, Palo Alto, CA 94306, USA; tiwari@lmsal.com
[2] Bay Area Environmental Research Institute, NASA Research Park, Moffett Field, CA 94035, USA
[3] SETI Institute, 339 Bernardo Ave., Mountain View, CA 94043, USA
[4] NASA Marshall Space Flight Center, Mail Code ST 13, Huntsville, AL 35812, USA
[5] Center for Space and Aeronomic Research, The University of Alabama in Huntsville, Huntsville, AL 35805, USA
[6] Rosseland Centre for Solar Physics, University of Oslo, P.O. Box 1029 Blindern, NO-0315 Oslo, Norway
[7] Institute of Theoretical Astrophysics, University of Oslo, P.O. Box 1029 Blindern, NO-0315 Oslo, Norway
[8] The Center for Astrophysics—Harvard and Smithsonian, 60 Garden St., Cambridge, MA 02138, USA
[9] University of Lancashire, Preston, PR1 2HE, UK
[10] Vanderbilt University, 2201 West End Ave., Nashville, TN 37235, USA
[11] Institute for Astronomy, University of Hawai'i at Mānoa, Pukalani, HI 96768, USA
[12] Montana State University, Culbertson Hall, 100, Bozeman, MT 59717, USA
Received 2025 October 5; revised 2025 November 13; accepted 2025 November 22; published 2025 December 11

Abstract

On 2024 April 17, the third successful Hi-C sounding rocket flight, Hi-C Flare, recorded coronal images in Fe XXI 129 Å emission from 11 MK plasma during the postmaximum phase of an M1.6-class solar flare, achieving unprecedented spatial (∼300 km) and temporal (1.3 s) resolutions. The flare started at 21:55 UT, peaked at 22:08 UT, and lasted ∼40 minutes. Hi-C observed for over 5 minutes (22:15:45–22:21:25), starting roughly 8 minutes after flare maximum. A sudden compact bright burst—875 ± 25 km wide, lasting 90 ± 1.3 s, exhibiting a proper motion of ∼ 50 km s^{-1}, and splitting into two toward the end—occurs near the foot of some postflare loops. Its size and brightness are reminiscent of flare-ribbon kernels during a flare's rapid rise phase, kernels marking sites of sudden heating and hot plasma upflow, making its occurrence during the late phase surprising. Such isolated brightenings in a flare's postmaximum phase are rare and have not been previously reported. The kernel was detected in all Solar Dynamics Observatory (SDO)/Atmospheric Imaging Assembly channels. Its 1600 Å light curve peaked ∼50 s earlier than its 131 Å light curve, similar to that of flare-ribbon kernels, albeit with a smaller delay of ∼25 s, during the impulsive phase of the flare. In SDO/Helioseismic Magnetic Imager magnetograms, the kernel sits in unipolar positive magnetic flux near an embedded clump of negative flux. Although localized magnetic reconnection within the kernel (a microflare) cannot be ruled out for its cause, the observations favor the localized brightening being an isolated, exceptionally late flare-ribbon kernel, resulting from an exceptionally late burst of the flare's coronal reconnection.

Unified Astronomy Thesaurus concepts: Solar flares (1496); Solar active regions (1974); Solar activity (1475); Solar active region magnetic fields (1975); Solar corona (1483); Solar coronal heating (1989); Magnetic fields (994); Solar extreme ultraviolet emission (1493)

Materials only available in the online version of record: animations

1. Introduction

The third successful sounding-rocket flight of the High-Resolution Coronal Imager (Hi-C 3, namely "Hi-C Flare": G. D. Vigil et al. 2025, in preparation) took coronal extreme-ultraviolet (EUV) images of NOAA active region (AR) 13645 in 129 Å (dominated by Fe XXI emission) with unprecedented spatial and temporal resolutions (∼300 km, 1.3 s). The data were collected for over 5 minutes, during the period of 22:15:41–22:21:25 UT on 2024 April 17, near solar disk center (AR position: S08E23). The Hi-C Flare captured a segment of the decay phase of an M1.6-class solar flare, about 8 minutes after the flare maximum. The images show a small-scale, localized, outstanding transient brightening at the outer edge of the flare. This type of isolated, small-scale, flare-kernel-like brightening during a flare's postmaximum phase has not been reported in previous coronal EUV observations.

Solar flares are one of the most complex challenges in astrophysics, with each new observation testing and advancing our understanding. Solar flares are thought to be powered by magnetic reconnection in stressed magnetic fields (e.g., K. Shibata et al. 1995; E. Priest & T. Forbes 2000; R. L. Moore et al. 2001; E. G. Zweibel & M. Yamada 2009; B. Joshi et al. 2011; A. O. Benz 2017). Many aspects of the reconnection process remain poorly understood—for example, the mechanisms of energy transport, the evolution of mass flows during the flare, and how a significant portion of the magnetic energy is converted into accelerated nonthermal particles. Solar flares emit radiation across a broad range of the electromagnetic spectrum (L. Fletcher et al. 2011). By their peak 1–8 Å soft X-ray flux observed by GOES, solar flares are categorized into

different classes. The energy released in different flare classes can be considered proportional to their peak GOES 1–8 Å flux. X-class flares are usually the most energetic, often releasing magnetic energy on the order of 10^{32} erg (A. G. Emslie et al. 2005), but can reach up to 10^{33} erg (A. G. Emslie et al. 2012; G. Aulanier et al. 2013; S. Toriumi et al. 2017) or even higher (T. Sakurai 2022). M-, C-, B-, and A-class flares release approximately 10^{31}, 10^{30}, 10^{29}, and 10^{28} erg, respectively (e.g., S. K. Tiwari et al. 2009, Appendix C).

The flare emission is predominantly from hot flare loops with temperatures exceeding 10 MK, which are anchored in bright chromospheric ribbons (S. Masuda et al. 1994; H. P. Warren & A. D. Warshall 2001; P. R. Young et al. 2013; D. R. Graham & G. Cauzzi 2015). As per the standard flare model, also known as CSHKP model (H. Carmichael 1964; P. A. Sturrock 1966; T. Hirayama 1974; R. A. Kopp & G. W. Pneuman 1976), these ribbons mark the footpoints of the reconnected magnetic field lines and are sites of intense energy deposition via accelerated particles, magnetic wave dissipation, and thermal conduction from the corona. The energy input leads to the evaporation of chromospheric plasma, which fills the newly reconnected coronal loops, forming the hot, dense structures observed in EUV and soft X-rays during the gradual phase of flares (A. O. Benz 2017).

Because flare emission is primarily associated with hot flare loops that have temperatures exceeding 10 MK, Hi-C Flare observations at 129 Å, with sensitivity to emission of plasma at temperatures over 10 MK plasma, are well able to capture such events with unprecedented high spatial and temporal resolutions. In the rapid rise phase of a solar flare, ribbon kernels can appear as localized brightenings that may exhibit apparent motions along ribbons driven by slipping magnetic reconnection (e.g., M. Janvier et al. 2013; J. Dudík et al. 2016; M. Sobotka et al. 2016). This initial brightening in flare loop feet provides crucial insights into the fundamental processes driving solar flares (A. O. Benz 2017).

While the rapid rise, main, and decay phases of solar flares have been the focus of numerous observational studies (W. J. MacCombie & D. M. Rust 1979; L. Fletcher et al. 2011; A. O. Benz 2017; Hinode Review Team et al. 2019, and references therein), the occurrence of flare-ribbon kernels during the postmaximum phase has rarely been reported (A. Czaykowska et al. 1999; M. Sobotka et al. 2016). One of the lesser-known topics in flare physics is the mechanism by which flares continue to be heated during their postmaximum phase (A. Czaykowska et al. 1999, 2001). Proposed explanations for such heating include prolonged magnetic reconnection (R. Moore et al. 1980; H. P. Warren 2006; K. K. Reeves et al. 2007; M. Kuhar et al. 2017), compression from strong downflows (K. K. Reeves et al. 2017; J. Unverferth & J. W. Reep 2023), shock heating (T. Yokoyama & K. Shibata 2001), or some combination of these. In this work, we report the observation of a prospective isolated flare-ribbon kernel during the postmaximum phase of a solar flare.

2. Data and Methods

The 5 minutes of Hi-C Flare observations, obtained at a cadence of 1.3 s and a spatial resolution of ∼300 km, were complemented by the Helioseismic Magnetic Imager (HMI; J. Schou et al. 2012) and Atmospheric Imaging Assembly (AIA; J. R. Lemen et al. 2012) on board Solar Dynamics Observatory (SDO; W. D. Pesnell et al. 2012).

A degradation in the instrument's spatial resolution from previous flights is expected as a result of the mirror recoating process. The resolution limit of the instrument is currently estimated to be ∼0.″45, and more detailed information on the actual spatial resolution of Hi-C 3 will be provided in the forthcoming instrument paper (G. D. Vigil et al. 2025, in preparation).

The full field of view (FOV) of Hi-C Flare was $2.'2 \times 4.'4$, as shown in Figure 1. Because the flare took place within the region outlined by the red dashed box in Figure 1(c), we studied that region in this work. Figure 2(a) spans this region of interest. The small red box in Figure 2(a) centers on the bright kernel that is under investigation. An animation of the Hi-C images is available (see Figure 2).

We use most SDO/AIA channels to follow the flare's evolution by creating animations and light curves. Through its seven EUV channels and two UV channels, SDO/AIA continuously takes 0.″6 pixel full-disk images of the solar atmosphere across a broad range of temperatures. The cadence is 12 s for EUV channels and 24 s for UV channels. In this study, we use all the EUV channels: AIA 304, 171, 193, 211, 335, 94, and 131 Å, which primarily detect emission from plasma at approximately 50,000 K (He II); 700,000 K (Fe IX/X); 1.5 MK (Fe XII); 2 MK (Fe XIV); 2.5 MK (Fe XVI); 6–7 MK (Fe XVIII); and 10–12 MK (Fe XXI), respectively. It should be noted that the AIA 94 and 131 Å channels are also sensitive to cooler plasma components, around 1 MK and 0.5 MK, respectively, while the AIA 193 Å channel includes a hotter contribution near 20 MK. In flares, the 171 channel contains a ≈20% contribution from free–free continuum emission (B. O'Dwyer et al. 2010). Additionally, the AIA 193 and 211 Å channels can detect some cooler plasma as well; see J. R. Lemen et al. (2012) for further details. We also use AIA 1600 Å UV images to follow the response of the lower atmosphere to reconnection-generated high-energy particles from the corona. The 1600 Å passband on AIA primarily captures lower-chromospheric continuum emission but also includes the two C IV lines near 1550 Å, which form at temperatures around 10^5 K in the lower transition region (TR). Short-term brightenings observed in the 1600 Å band have been attributed to these C IV lines, indicating that such emission originates from the lower TR (J. R. Lemen et al. 2012).

After carefully inspecting the AIA images, we found that the despiking process applied during the preparation of AIA Level 1.5 files to remove signals of cosmic particles also removed some small-scale brightenings, including a portion of the bright kernel that is central to our analysis. To address this, we respiked six AIA EUV wavelengths (131, 94, 171, 193, 211, and 335 Å) and performed our analysis on the respiked images. To enable readers to compare the appearance of the bright kernel in despiked and respiked AIA 131 Å images, as well as in other channels, we provide an animation that combines 30 minutes of respiked data followed by 2 hours of despiked data.

Figure 3 compares the effective areas as a function of wavelength for the AIA 131 and Hi-C 129 channels, along with their corresponding temperature responses. It is evident that the AIA 131 channel is more strongly contaminated by cooler emission from Fe VIII compared to Hi-C 129. The temperature response of the Hi-C 129 channel is about 2.5 times less sensitive to cooler emission than that of AIA 131. Therefore, the brightenings observed in Hi-C are more likely from hotter plasma.

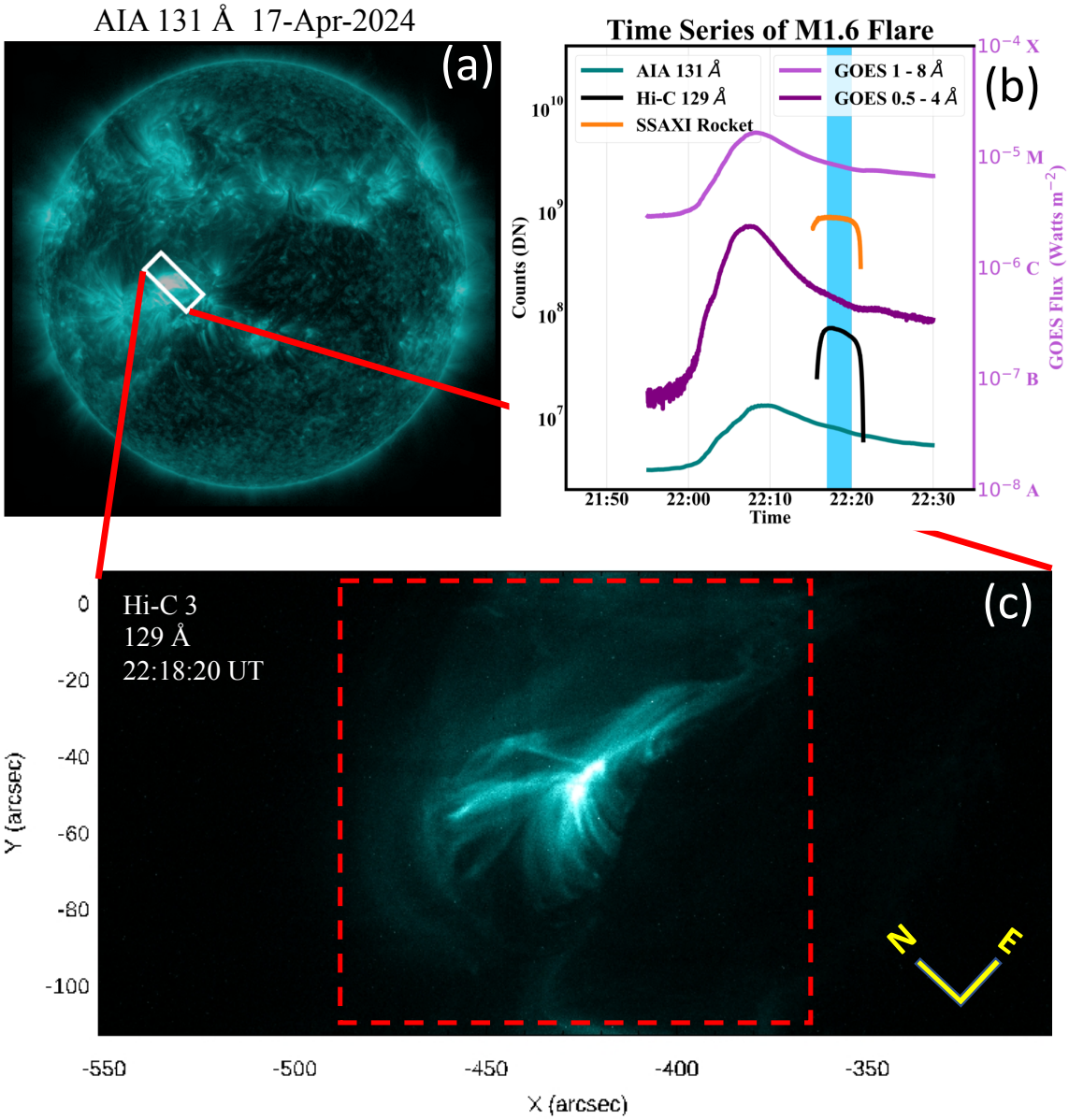

Figure 1. Context image of Hi-C Flare observations of NOAA AR 13645 at the solar disk position S08E23. Panel (a) shows full-disk solar image from SDO/AIA in the 131 Å channel. A white box roughly outlines the region observed by Hi-C for over 5 minutes, a frame of which is shown in panel (c). Panel (b) shows GOES, AIA, Hi-C, and SSAXI-Rocket light curves of the observed flare. The shade in cyan color outlines the timing of the main phase of Hi-C observations. Panel (c) shows an image frame with the full field of view (FOV) observed by Hi-C Flare in 129 Å. The dashed red box outlines the region with most activities and is used for further analysis. The faint grid structure on the Hi-C image is an artifact of focal plane filter shadow that still remains in the data. The directions of solar north and east are indicated in the lower-right corner of panel (c).

The Hi-C Flare campaign included the following instruments: Hi-C 3 (passband centered at 129 Å, sensitive to the hot coronal plasma at ∼11 MK); COOL-AID: EUV slitless spectrograph centered on 129 Å; CAPRI-SUN (High Cadence Low-energy Passband X-Ray Detector with Integrated Full-SUN FOV): student-built full-Sun soft X-ray detector with rapid cadence (1000 times faster than GOES); and SSAXI-Rocket (C. S. Moore et al. 2024): compact soft X-ray imager.

This Letter presents the first result from Hi-C 3 data. Data from other Hi-C Flare instruments are still under evaluation and are not considered here.

Interface Region Imaging Spectrograph (IRIS) and Hinode were observing a different target, as originally planned the previous day (s) before the flight, but during the flight, the flare occurred in a different AR to which Hi-C was repointed. So, unfortunately, coordinated data from IRIS and Hinode were not obtained for this flare.

To process the data, first we coaligned Hi-C Flare 129 Å images and AIA 131 Å images, as the passbands for the two are similar (Figure 3). For this, we rotated SDO images by about 45° counterclockwise and compared the images from Hi-C Flare and AIA 131 and applied any further shifts needed by performing a cross correlation. Then, the other AIA images and the HMI line of sight (LOS) magnetograms were given the same rotation and shifts.

3. Results and Discussion

Figure 1 provides an overview of the Hi-C Flare observations, showing the full FOV recorded by Hi-C and the FOV of

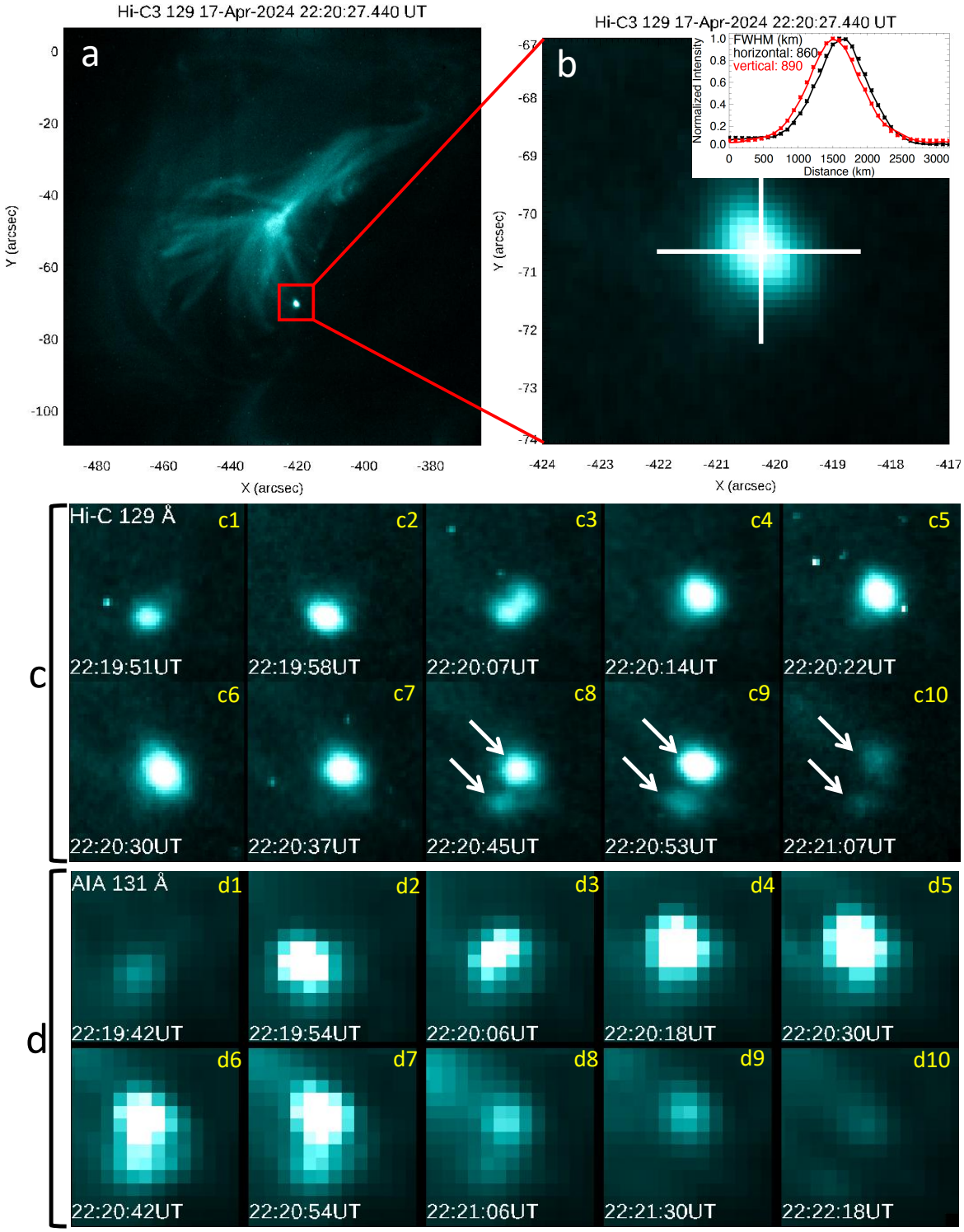

Figure 2. Overview and evolution of the fine-scale bright kernel. Panel (a) contains an image displaying the region of interest of the Hi-C Flare observations. A zoomed-in view of the localized brightening is shown in panel (b). An inset in panel (b) presents two plots showing the intensity profiles along two orthogonal cuts through the kernel, as indicated by the white lines, with Gaussian fits overplotted on the intensity profiles as asterisks. This plot is made to measure the size/diameter of the kernel. The lower two sets of rows, marked by (c) and (d), each contain two rows of Hi-C Flare 129 Å images and AIA 131 Å images, respectively, showing the evolution of the bright kernel. The size of each image in panels (c) and (d) is $7'' \times 7''$. The difference in appearance of the brightening in panels (c) and (d) arises from the disparity in the spatial resolutions of the two instruments. Note that the time stamps of the respective images on Hi-C and AIA are not identical—the AIA 131 Å images span a somewhat longer time period. Arrows in panels (c8), (c9) and (c10) mark the splitting of the kernel into two parts, due to the two loop feet being involved, most clearly visible at 22:20:49 UT in the Hi-C 3 animation. An animation of panel (a) is available, and it runs for 7 seconds.

(An animation of this figure is available in the online article.)

Figures 2(a) and 4. The accompanying GOES X-ray plots summarize the M1.6-class flare and indicate the time interval of the flare segment captured by Hi-C. The distribution of the flare loops suggests the flare occurred in a fan-spine topology (e.g., S. Masson et al. 2009; X. Sun et al. 2013; M. Janvier et al. 2016). The flare loops follow a distinct dome shape,

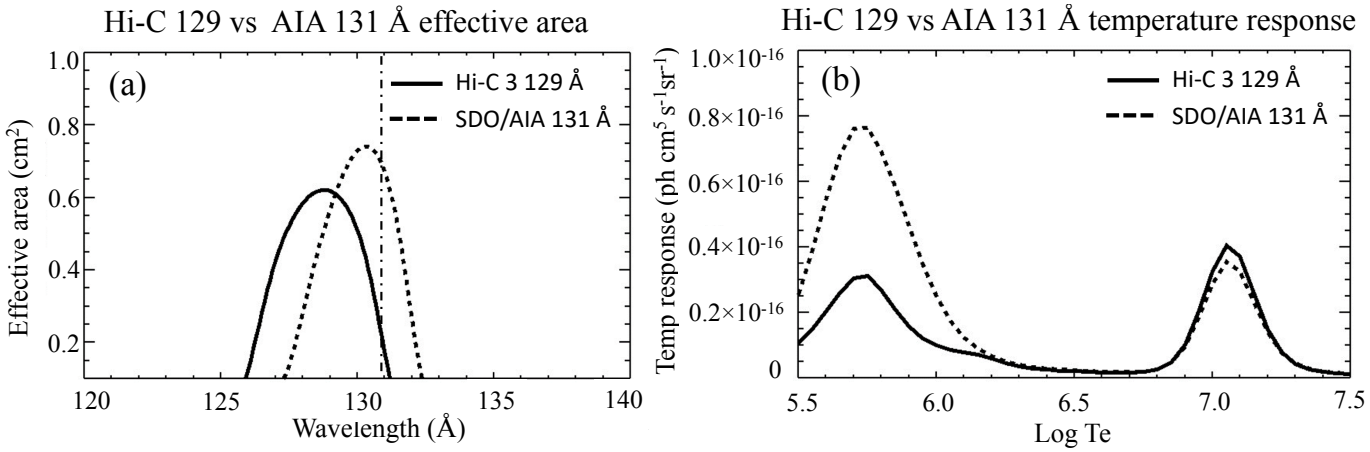

Figure 3. Comparison of Hi-C 129 and AIA 131 channel characteristics. Panel (a): the effective area of the Hi-C 3 129 Å passband (solid) and AIA 131 Å channel (dashed). A vertical dashed–dotted line marks the wavelength location of Fe VIII (∼131 Å). Panel (b): the temperature response of Hi-C 129 Å (solid) and AIA 131 Å (dashed). At the cooler temperature peak (log $T_e = 5.7$), AIA is about 2.5 times more sensitive than Hi-C, whereas both are nearly equally sensitive to hotter plasma at the peak of log $T_e = 7.05$.

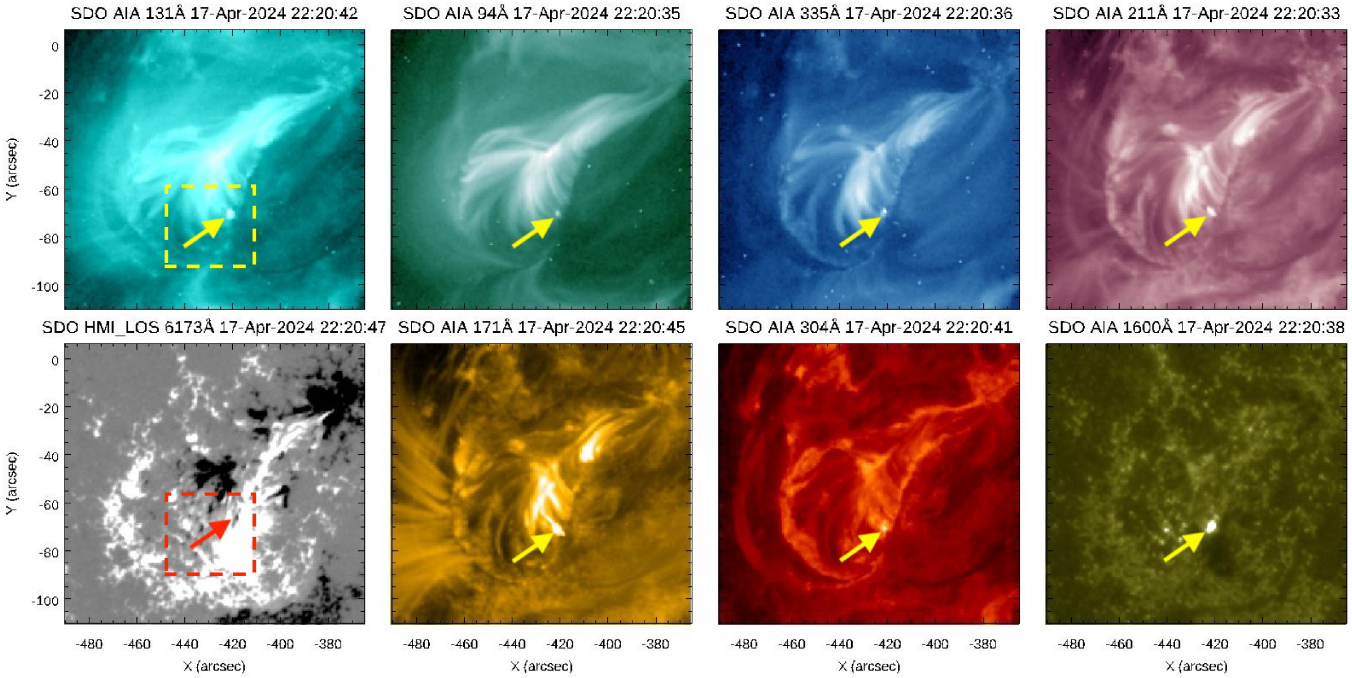

Figure 4. SDO observations of the M1.6-class flare are shown in various AIA channels, along with the HMI line-of-sight magnetogram. An arrow in each panel points to the location of the bright kernel under investigation. A boxed region covers two locations of similar brightenings: one captured by both Hi-C Flare and SDO, and the other observed only by SDO, approximately 6 minutes after the Hi-C Flare observations concluded. Both brightenings are shown in Figure 5. An animation displaying all these panels, first showing the flare in respiked AIA images for about 30 minutes and then in despiked images for about 2 hours, is available. The total duration of the animation is 1 minute and 15 s.

(An animation of this figure is available in the online article.)

rooted in a semicircular ribbon, and extend along a spine rooted at $X \approx -370''$, $Y \approx -20''$.

Figure 2 shows the Hi-C region covering the flare, along with the localized brightening, the prospective bright flare-ribbon kernel, analyzed in detail. Regardless of its origin (whether a microflare or a localized flare-ribbon kernel, unless otherwise specified), we refer to this brightening simply as the bright kernel. Near its peak intensity, the kernel's diameter is estimated to be 875 ± 25 km, obtained by averaging its horizontal and vertical extents as illustrated in Figure 2(b). The measurement uncertainties in each direction were determined by measuring the diameter along three adjacent lines of pixels along the two orthogonal cuts shown in Figure 2(b). Since the two orthogonal extents are similar and the kernel appears roughly circular, we averaged the two measurements and their associated uncertainties to define its diameter. The measured diameter represents an upper limit, and the true size of the kernel could be smaller. In particular, any substructure on scales below the telescope's point-spread function (≃0.″45; K. Kobayashi et al. 2014; L. A. Rachmeler et al. 2019; G. D. Vigil et al. 2025, in preparation) would not be resolved in these observations. The size of the bright kernel is comparable to that of typical flare-ribbon kernels. For example, P. Romano et al. (2017) reported that circular ribbons in flares are

composed of several adjacent compact kernels with sizes of about 1″–2″. We note that smaller flare-ribbon kernels are detected in higher-resolution observations (e.g., V. Singh et al. 2025; J. Thoen Faber et al. 2025; R. Yadav et al. 2025).

The evolution of the kernel in the Hi-C Flare 129 Å images (Figure 2(c)) and their light curves (described later in this section) reveal that the kernel lived for 90 ± 1.3 s. In the Hi-C and SDO animations, there is evidence of magnetic field restructuring in the corona associated with the kernel (compare Hi-C image frames, for example, at 22:18:40 and 22:19:51 in the Hi-C animation accompanying Figure 2), suggesting coronal magnetic reconnection during the brightening. Furthermore, the Hi-C brightening showed a subtle north–west motion between 22:20:00 and 22:20:15 UT, with a plane-of-sky speed of about 50 km s^{-1}. These observed dynamics align with the apparent motions of flare kernels attributed to slipping reconnection (e.g., J. Dudík et al. 2014; T. Li & J. Zhang 2015; J. Lörinčík et al. 2019).

During its evolution, the kernel splits in two, particularly at the end (see panels (c8)–(c10)). In Figure 2(d), the evolution of the kernel is also shown in the AIA 131 Å channel, the AIA channel closest to the 129 Å of the Hi-C Flare images. The AIA 131 images also show splitting of the kernel in two at the corresponding times (see panels (d7) and (d8)). When viewed closely in the SDO animation (Figure 4), there appear to be two upward-reaching coronal loop legs (see in the animation frames near time 22:20:30 UT in AIA 131, 94, 211 and 171 Å), one rooted in each of these two kernels. Apparently, when the whole kernel was very bright, the two parts appeared to be merged and looked like a single kernel, and with time, during cooling, the two loop feet separate into the two bright kernels. Perhaps these two kernels and their corresponding loop legs are a result of the evolution of the magnetic field. These two loop feet can be seen separated in the Hi-C 129 Å animation (see near 22:20:30 UT and at 22:20:49 UT), as well as in the AIA 131 Å image shown in Figure 5(a).

Splitting and merging kernels have been seen before in flare ribbons in the beginning of a C-class solar flare in Ca II H interference filter images centered on 3968 Å by M. Sobotka et al. (2016) using high-resolution GREGOR data. As a result of the splitting and merging interrupting the tracking, these "knots" were not followed during their whole lifetime. Their tracking periods ranged from 32 to 86 s for different knots having lifetimes of about a minute. These values are similar to the lifetime of our bright localized kernel, and their knots show splitting and merging, like that in our case. Similar footpoint motions were observed by J. Qiu et al. (2002) in UV and EUV images but again in flare kernels in the beginning of a solar flare.

We note that A. Czaykowska et al. (1999) were the first to report chromospheric evaporation in TR and coronal lines during the late gradual phase of a flare. Their conclusion, based on the observed upflows and downflows, implied that reconnection was ongoing throughout their flare observations. Flare-ribbon kernels extending over a sunspot umbra were later reported by M. Sobotka et al. (2016). In contrast to our isolated bright kernel, both of these studies involved fully developed flare ribbons during the decay phase of M- and C-class flares, respectively.

A second localized brightening occurs slightly southeast of the above kernel about 5 minutes later. This second kernel was not captured by Hi-C Flare, but it shows striking similarity with the first one in SDO data. In Figure 5, we display SDO/AIA 131 Å images with LOS magnetic field contours on them, together with the corresponding contoured LOS magnetograms. The FOV covers both kernels. This figure shows that each kernel is located near the edge of a negative polarity patch in a dominant positive magnetic polarity region. The neutral line nearest the kernel in each case is not sharp, and Hi-C and AIA images show no obvious extensions toward the opposite-polarity magnetic flux patch. This suggests the origin of this fine-scale heating event may not be by magnetic reconnection in the lower atmosphere that often accompanies flux cancellation, as seen for small-scale dots, tiny loops, and small surges by S. K. Tiwari et al. (2019) and small-scale jets by N. K. Panesar et al. (2019) using data from Hi-C 2.1 (L. A. Rachmeler et al. 2019). Nonetheless, given the nearness to the neutral line, that cannot be strongly concluded. For example, the TR images from IRIS in S. K. Tiwari et al. (2019) show an extended intensity structure reaching the smaller, bright dot-like heating events seen in Hi-C 2.1 172 Å images.

Somewhat similar coronal brightenings above flux cancellation were also recently reported in the synthetic images of Si IV 1400 Å of a Bifrost MHD simulation (S. K. Tiwari et al. 2022). In Fe IX/X images, the brightenings were smaller than the corresponding extended structures in Si IV synthetic images. It was concluded that only the hottest counterpart of magnetic reconnection in the lower atmosphere showed up in Fe IX/X emission, while the lower, more dense atmosphere showed larger structures in the Si IV line. Unfortunately, in the absence of coordinated IRIS observations for this flare, we cannot determine whether a similar extended structure was present in the TR and therefore cannot test the possibility of magnetic reconnection as the cause of the localized fine-scale hot kernel.

The emission measure (EM) maps in Figure 6, calculated using six AIA channels [94, 131, 171, 193, 211, 335] using the method described in M. C. M. Cheung et al. (2015), reveal that the bright kernel is multithermal in nature. This is consistent with previous studies reporting multithermal emission at flare loop footpoints, for example, manifested by multipeaked differential emission measure distributions (e.g., G. Del Zanna et al. 2011; D. R. Graham et al. 2013; M. B. Kennedy et al. 2013).

Somewhat similar hot, localized bright kernels were reported by R. O. Milligan & B. R. Dennis (2009) using Hinode/EUV Imaging Spectrometer Fe XXIII and Fe XXIV lines (formed at >12 MK) at a loop footpoint but again during the impulsive phase of a C-class flare. To the best of our knowledge, such hot, localized bright kernels during the postmaximum phase of a solar flare have not previously been reported.

To find out if the bright kernel gives luminosity curves similar to flare-ribbon kernels, we created light curves for different AIA channels together with the Hi-C 129 Å light curves. Figure 7(a) shows light curves for the larger FOV, covering the whole AR, for reference. As is usual in solar flares, AIA 1600 Å peaks first, displaying the first response to impulsive downstreaming charged particles from reconnection. Furthermore, AIA 1600 Å shows two peaks, likely corresponding to two successive streams of charged particles. The AIA 304, 171, 193, 211, and 335 Å channels also exhibit intensity enhancements nearly concurrently with the two 1600 Å peaks. Later, the 131 Å channel peaks, then the 94 Å

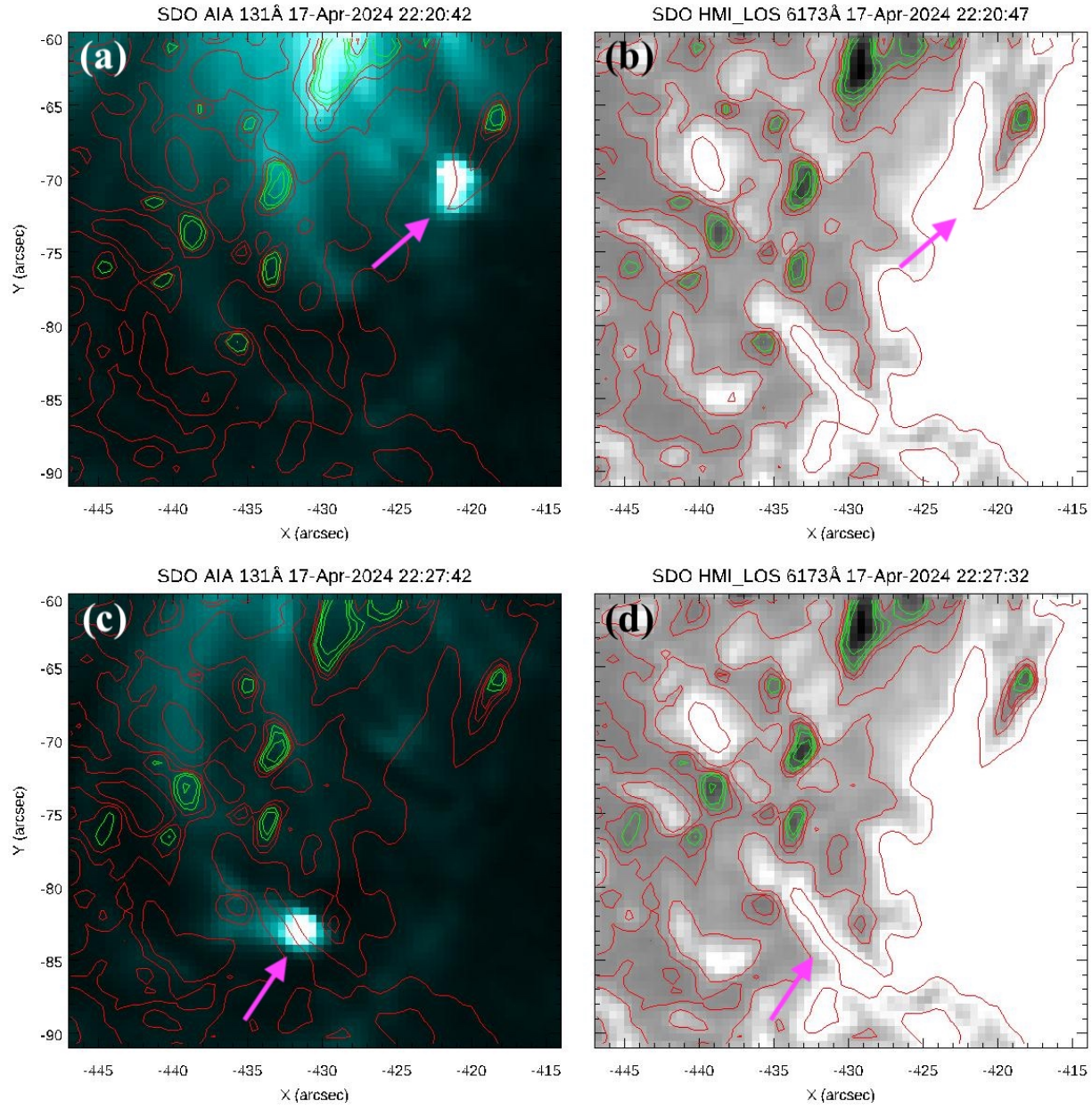

Figure 5. Magnetic field distribution at and near two bright kernels. Panel (a): SDO/AIA 131 Å image during the localized brightening activity—this event is captured by Hi-C Flare. An arrow in pink points to the bright kernel. The corresponding HMI LOS magnetic field is shown on the right in panel (b), displaying the magnetic field distribution. The red and green contours, also overplotted on panel (a), correspond to positive and negative polarity, respectively, with contour levels of [±20, ±60, ±150, ±500] G. The bottom panels, (c) and (d), are the same as the top two but for a different time (about 5 minutes later than the top ones), showing a second similar brightening event, outside the Hi-C observation time, and so only captured by SDO. The dashed yellow or red box in each of Figure 4 panels showing the AIA 131 and HMI LOS magnetogram outlines the FOV of these images. An animation is available, with a total duration of 15 s.
(An animation of this figure is available in the online article.)

channel, and then consecutively later luminosity enhancements in the 335, 211, 193, and 171 Å channels, that is, the normal cooling sequence for flares, are seen. The first and second peaks in AIA 1600 Å luminosity occur approximately 300 s and 150 s before the peak of the 131 Å luminosity, respectively. We note that the uncertainty in SDO/AIA pixel EUV brightness, which depends on the gain of the CCD, is significantly smaller than the individual peaks of the light curves. Please see Table 6 of P. Boerner et al. (2012) for the camera-CCD gain and read noise.

Panel (b) of Figure 7 shows light curves of the small box covering the bright kernel in Figure 2. Similar to the light curves during the impulsive phase of the flare, the localized brightening curves show that 1600 Å peaks first. Immediately afterwards (within about 30–50 s), Hi-C 129 Å and all other AIA channels reach their peak intensities. Because the FOV does not include the loops, a subsequent cooling sequence is not observed. We judge that these light curves are consistent with this localized brightening being the footpoint of an isolated new flare loop. The AIA 1600 Å luminosity peaks approximately 50–60 s earlier than the AIA 131 Å luminosity peak. Such early peaking of the 1600 Å emission in solar flares, seen in panels (a), (b), and (c) of Figure 7, has been well observed by J. Qiu & R. Fleming (2025 and references therein).

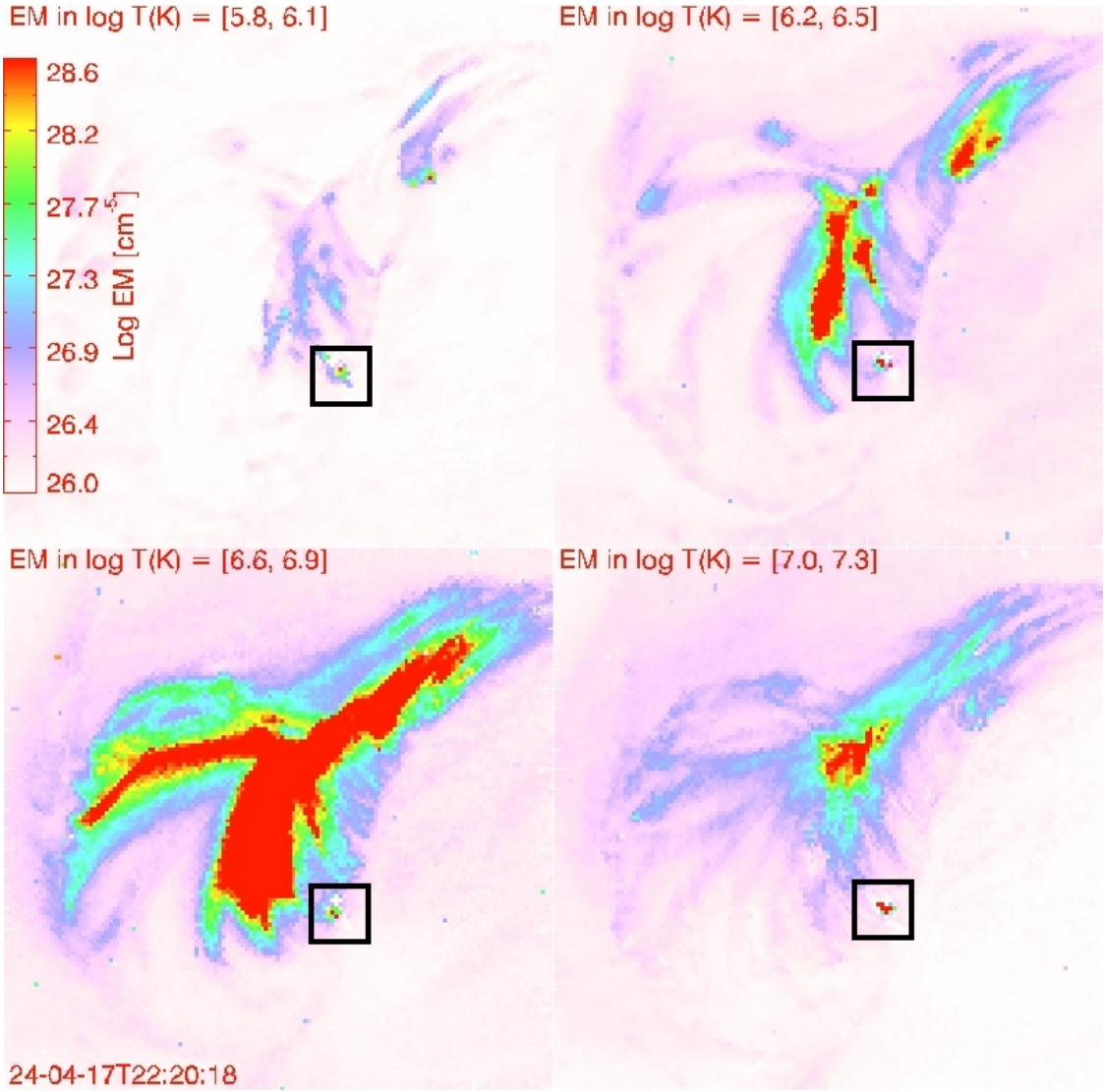

Figure 6. Emission measure (EM) maps created from six AIA channels [94, 131, 171, 193, 211, 335], displayed in four log temperature ($\log_{10}T$) bins for a given time (22:20:18). The black box in each panel centers on the bright kernel. The kernel carries significant EM in all temperature bins, thus representing its multithermal nature. An animation is available, with a total duration of 15 s.

(An animation of this figure is available in the online article.)

Panel (c) in Figure 7 shows AIA light curves of a flare-ribbon kernel during the impulsive phase of the flare. Similar to the light curves in the bright kernel observed by the Hi-C, the 1600 channel peaks first. However, the time difference between the 1600 peak and the subsequent 131 peak is shorter (by about 25 s) than that observed for the bright kernel in panel (b). This is the case for several of the bright kernels inspected —1600 peaks about 25 s before 131 does. Nonetheless, this observation supports the interpretation that the bright kernel under study is indeed an isolated, localized, flare-ribbon kernel. A caveat is that a local-reconnection burst can also produce such a delay, as the current sheet may extend to higher altitudes and heat less dense plasma, resulting in a similar scenario.

There is the presence of similar localized brightenings at multiple occasions before the flare started, also previously reported in other solar flares, e.g., by B. Joshi et al. (2011); see, for example, the animation accompanying Figure 4, at and around AIA 131 times of 21:22:54, 21:28:54, 21:35:18, 21:36:42, 21:40:54, 21:42:54, and 21:52:42, but only one (at 22:44:54) is seen after the flare has ended. Because the magnetic field distribution on the photosphere and field's general configuration remains somewhat similar, as seen in the animation accompanying Figure 5, we judge that these localized brightenings are most likely a result of streamed charged particles from a coronal magnetic reconnection. After the flare has ended, the magnetic field relaxes toward a more potential state, causing local coronal reconnection events to cease. Further, the light curves of similar bright kernels during the impulsive phase of the flare show a similar behavior as the light curves for the localized bright kernel seen by Hi-C.

While localized small-scale flare kernels in flare ribbons, sometimes referred to as "knots," as mentioned previously, are common and expected per standard flare models to occur during the initial phase of a solar flare (I. N. Sharykin & A. G. Kosovichev 2014; M. Sobotka et al. 2016; P. R. Young 2024; J. Thoen Faber et al. 2025; R. Yadav et al. 2025), their presence during the decay phase in EUV

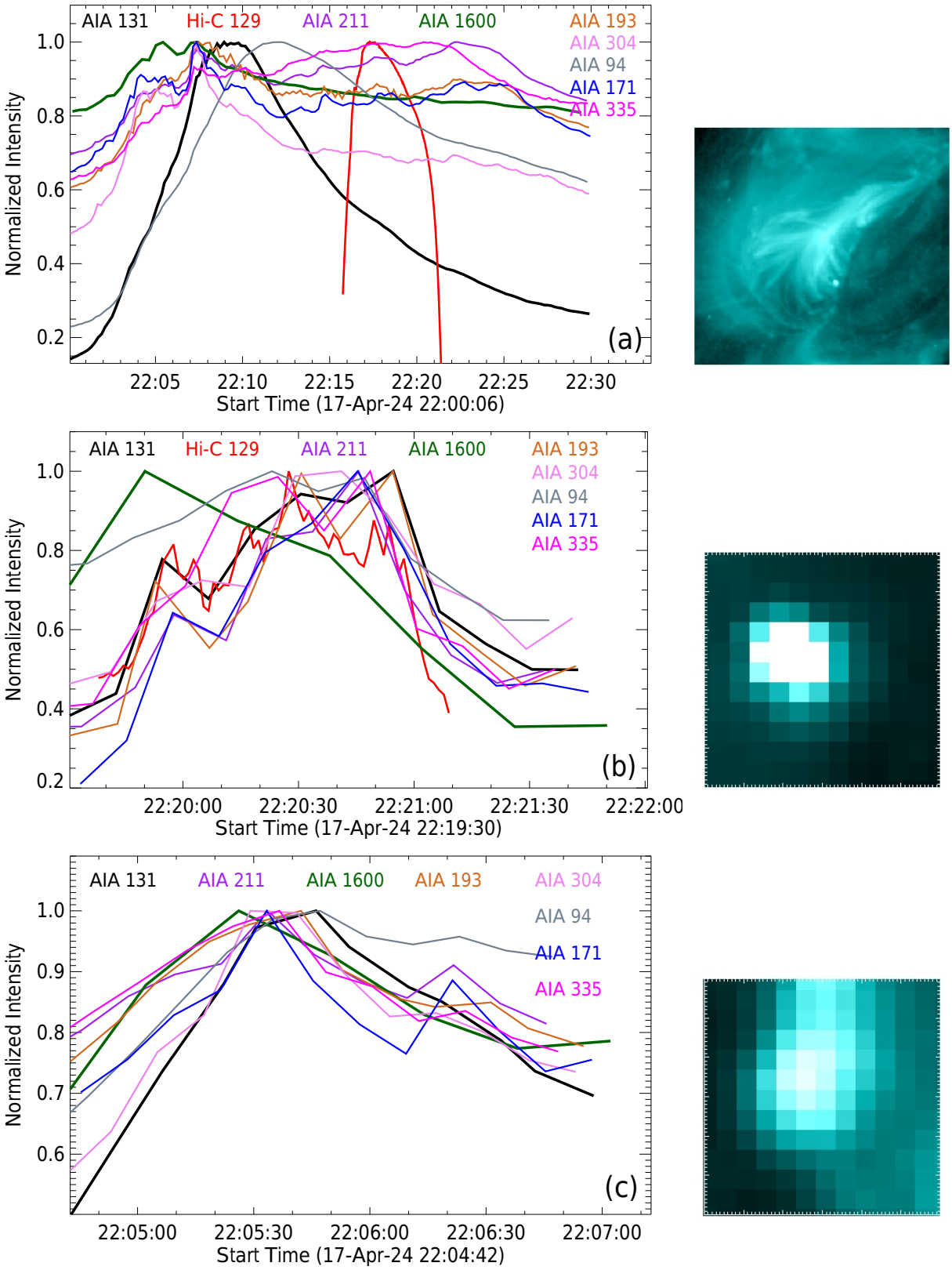

Figure 7. Light curves from SDO/AIA and Hi-C Flare data. Panel (a) shows light curves for the full FOV shown in Figure 2(a). Panel (b) shows light curves for the bright kernel in the FOV shown in Figure 2(b). Panel (c) shows light curves of different AIA channels of a localized flare-ribbon kernel during the impulsive phase of the flare. Insets to the right of each panel show the region, each in AIA 131 channel, for which the corresponding light curves were created. Each light curve in the figure is colored to match its corresponding wavelength annotation or legend. The light curves of 1600 and 131 are made thicker for easy distinction.

observations has not been reported before. I. N. Sharykin & A. G. Kosovichev (2014) explained their observed fine structuring of flare ribbons by Joule dissipation if the electrical resistivity is enhanced in the partially ionized plasma of the lower solar atmosphere or by turbulent resistivity due to even smaller structuring. These mechanisms perhaps apply to the

localized bright kernel we observe here in the postmaximum phase of the flare.

We note that, although not previously reported, isolated bright kernels during a flare's gradual phase may not be uncommon; however, contamination from cooler emission can reduce their contrast, making them harder to detect in AIA 131 Å. This feature might have been less apparent without the Hi-C data (see Figure 3).

Our inference that the brightening is a flare kernel in the late phase is consistent with the idea of prolonged reconnection for a prolonged heating in solar flares (A. Czaykowska et al. 1999, 2001; H. P. Warren 2006; K. K. Reeves et al. 2007; J. Qiu et al. 2012; J. W. Reep et al. 2020). Bursty reconnection (e.g., V. M. Nakariakov & V. F. Melnikov 2009) in coronal loops after the main phase of a flare plausibly makes localized flare-ribbon bright kernels in the late phase. We think this is what is happening in our current observation.

In a time–distance map (not shown), we found no evidence of plasma downflows along the loop leg to the bright kernel. This indicates that the localized brightening was unlikely caused by impact compression from a downflow (K. K. Reeves et al. 2017).

The present Hi-C Flare observations raise several questions: How common is the occurrence of isolated flare kernels during the postmaximum phase? Is it more prevalent in M-class flares than in other classes, such as X-class or C-class flares? Why is the brightening so highly localized? Why did neighboring coronal loops not participate in the reconnection, forming an extended flare ribbon as seen in the impulsive phase? Future MHD simulations should seek to account for the presence of such fine-scale kernels during the flare postmaximum phase. Perhaps a flare's impulsive/rise and maximum phases are a storm of fine-scale bursts of reconnection in the flaring coronal magnetic field (R. P. Lin et al. 1984), each burst being similar to the burst that made either of the two bright kernels reported here.

3.1. A "Late-phase Localized Flare-ribbon Kernel" or a "Microflare"?

Based on the discussions in Section 3, here we make a list of observational support for each of the two scenarios.

3.1.1. Support for the Kernel Being a Localized Flare-ribbon Kernel Caused by Coronal Magnetic Reconnection

1. As noted earlier in Section 3, many similar localized brightenings occurred at or near the same location as the brightening under study, prior to the flare. See, for example, in the animation accompanying Figure 4, the AIA 131 Å images at and around 21:22:54, 21:28:54, 21:35:18, 21:36:42, 21:40:54, 21:42:54, and 21:52:42. But only one such brightening (at 22:44:54) is observed after the flare has ended. Since the photospheric magnetic field distribution remains largely unchanged (see the animation accompanying Figure 5), we infer that these localized brightenings are likely caused by streams of charged particles from coronal magnetic reconnection. After the flare, the field becomes less nonpotential (i.e., more potential), causing coronal reconnection to cease.
2. The localized brightenings do not show a preference for mixed-polarity regions, as would be preferred by a microflare event. Several of the brightenings noted above are seated at unipolar magnetic regions, as is characteristic for flare ribbons.
3. Further, the light curves of similar bright kernels during the impulsive phase of the flare show a similar behavior to the light curves for the localized bright kernel seen by Hi-C. The uncertainty in pixel EUV brightness, which depends on the CCD gain, is much smaller than the peak intensities in the light curves. This readout error is particularly low for AIA (P. Boerner et al. 2012). We verified that, for all AIA channels, the uncertainties are significantly smaller than the observed peaks in the light curves.
4. There is no *sharp* polarity inversion near the bright kernel. We think that favors the idea that the kernel was made by some mechanism other than local reconnection in a microflare.
5. That the kernel is at the foot of a loop leg that extends toward the spine of the AR suggests its brightening results from reconnection in the corona. Evidence of magnetic field restructuring in the cusp of flare loops that include the loop rooted in the kernel also favors this interpretation.
6. The bright kernel is also unlikely to be a small bipole without coronal temperatures, as, for example, seen in 1600 Å by S. K. Tiwari et al. (2014). As previously mentioned, the magnetograms do not show an obvious polarity inversion line or both polarities of a bipolar system. Further, Figure 3 shows that Hi-C 129 is less sensitive to cooler plasma than AIA 131; therefore, its clear visibility in Hi-C supports the interpretation that the bright kernel has coronal temperatures.

3.1.2. Support for the Kernel Being a Localized Reconnection Microflare Event

1. The bright kernel is much brighter than other similar localized brightenings, and so, even if others may be generated by coronal magnetic reconnection, this kernel could be caused by a local magnetic reconnection.
2. In previous observations of Hi-C 2.1 (S. K. Tiwari et al. 2019) and Solar Orbiter's Extreme Ultraviolet Imager/High Resolution Imager, as well as in simulations (S. K. Tiwari et al. 2022), an extended structure like jet spire from the reconnection site has been observed in TR temperatures. In the absence of IRIS observations, a scenario of local magnetic reconnection, e.g., producing a jet from the kernel, cannot be ruled out.
3. A sharp polarity inversion line might not be necessary for a local-reconnection microflare to occur. Magnetic reconnection can happen as a standing current sheet, starting from or extending to the higher atmosphere (V. Hansteen et al. 2019).
4. In the HMI magnetograph, scattered light might hide few-pixel clumps of opposite-polarity flux that are inside a larger area of unipolar flux as strong as that surrounding our kernel (see, e.g., Y. M. Wang 2016; N. K. Panesar et al. 2018, 2019).
5. There is no obvious conjugate footpoint to the localized bright kernel. However, a conjugate flare loop footpoint may sometimes be too spread out to be distinctly visible, particularly in such a localized coronal reconnection event as ours. Alternatively, the conjugate footpoint may

sometimes get obscured by flare emission in the corona along the line of sight. Finally, not all flare-ribbon kernels have a conjugate kernel that shows corresponding intensity and velocity evolution (see, e.g., Section 3 of M. Sobotka et al. 2016).

In our view, these points favor interpreting the bright kernel as a flare-ribbon kernel produced by a burst of coronal magnetic reconnection. Nonetheless, the arguments in Sections 3.1.1 and 3.1.2 do not definitively confirm either scenario.

4. Conclusions

We report the observation of a fine-scale, localized bright kernel during the postmaximum phase of an M1.6-class solar flare, captured in 129 Å hot emission (∼11 MK) by the first Hi-C Flare rocket flight experiment (the third successful Hi-C flight). This brightening lasted for about 90 ± 1.3 s and had a diameter of at most 875 ± 25 km. SDO/AIA 131 Å images reveal a second, similar brightening approximately 5 minutes later at another location. In SDO/HMI LOS magnetograms, each of these bright kernels is in positive unipolar flux but near an inclusion of negative flux—suggesting the possibility of a burst of local magnetic reconnection being the cause. However, various observational facts favor the bright kernel being a localized bright flare-ribbon kernel produced by accelerated charged particles from coronal magnetic reconnection.

Several qualitatively similar brightenings were observed in the same or nearby locations before and during the flare. Such activity in this region, on the other hand, declined after the flare gradual phase. This suggests that these localized brightenings were manifestations of a response of the lower atmosphere to heating driven by flare reconnection acting in the conversion of free energy accumulated in the corona. All of these brightenings, including the one observed by Hi-C, were located at the footpoints of flare loops, the defining characteristic of flare kernels. These flare loops constitute the dome of the fan-spine topology, directed toward the likely location of a null point at the dome apex. Furthermore, the Hi-C brightening exhibited an inconspicuous motion toward the northwest between 22:20:00 and 22:20:15 UT, at the plane-of-sky speed of about 50 km s^{-1}. Such dynamics are consistent with the apparent flare kernel motions driven by slipping reconnection (e.g., J. Dudík et al. 2014; T. Li & J. Zhang 2015; J. Lörinčík et al. 2019). And finally, the AIA 1600 Å light curves peaked about 50 s before the 131 Å emission. Inspection of light curves of several flare-ribbon kernels reveals a similar trend in that 1600 Å peaks about 25 s before 131 Å peaks. The arguments above provide further evidence that the structure observed by Hi-C is a late-phase isolated flare-ribbon kernel, resulting from coronal magnetic reconnection and the consequent impact of accelerated charged particles in the lower atmosphere.

We note, however, that the TR emission dominating the 1600 Å channel in flares responds very rapidly to flare heating from high altitudes irrespective of the heating agent (see, e.g., J. Lörinčík et al. 2025), i.e., whether the heating is by nonthermal particles, heat conduction, or by waves from the burst of coronal reconnection, or by a local burst of reconnection (microflare) low in the local magnetic field.

This Letter gives a first report of a prospective isolated, localized, multithermal, flare-ribbon kernel in the late phase of a solar flare. As each flare is unique, the prevalence of this phenomenon remains to be determined. Future Hi-C Flare flights and similar observations, ideally coordinated with IRIS, Hinode, Solar Orbiter, MUSE, and DKIST, should provide decisive insight into the cause of these localized flare kernels across different solar flares, thereby establishing their role in the postmaximum phase, and the entire flare process.

Acknowledgments

We thank the referee for insightful comments, which have helped improve the presentation of this Letter. We also express our gratitude to Paola Testa and Meng Jin for their valuable discussions on the readout error estimates for the AIA channels. S.K.T., N.K.P., and R.L.M. gratefully acknowledge support by NASA HSR grant (80NSSC23K0093), and NSF AAG award (no. 2307505). S.K.T. also aknowledges support by NASA contract NNM07AA01C (Hinode). N.K.P. acknowledges support from NASA's SDO/AIA grant (NNG04EA00C) and HSR grant (80NSSC24K0258). R.L.M. acknowledges the support from the NASA HGI program. J.L. and V.P. acknowledge support from NASA's HGI grant 80NSSC24K0553. J.L., V.P., and B.D.P. gratefully acknowledge support from NASA contract NNG09FA40C (IRIS). B.D.P. was supported by grant 80NSSC23K0164. We acknowledge the High-resolution Coronal Imager (Hi-C Flare) instrument team for making the flight data available under NASA Heliophysics Flight Opportunities for Research and Technology (HFORT) Low Cost Access to Space (LCAS) program (proposal HFORT19-0025). MSFC/NASA led the mission with partners including the Smithsonian Astrophysical Observatory, the University of Central Lancashire, and Lockheed Martin Solar and Astrophysics Laboratory. Hi-C Flare was launched on 2024 April 17. The AIA and HMI data are courtesy of NASA/SDO and the AIA and HMI science teams.

ORCID iDs

Sanjiv K. Tiwari https://orcid.org/0000-0001-7817-2978
Navdeep K. Panesar https://orcid.org/0000-0001-7620-362X
Ronald L. Moore https://orcid.org/0000-0002-5691-6152
Sabrina L. Savage https://orcid.org/0000-0002-6172-0517
Amy R. Winebarger https://orcid.org/0000-0002-5608-531X
Genevieve D. Vigil https://orcid.org/0000-0002-7219-1526
Juraj Lörinčík https://orcid.org/0000-0002-9690-8456
Vanessa Polito https://orcid.org/0000-0002-4980-7126
Bart De Pontieu https://orcid.org/0000-0002-8370-952X
Leon Golub https://orcid.org/0000-0001-9638-3082
Ken Kobayashi https://orcid.org/0000-0003-1057-7113
Patrick Champey https://orcid.org/0000-0002-7139-6191
Jenna Samra https://orcid.org/0000-0002-4498-8706
Anna Rankin https://orcid.org/0009-0002-8726-6196
Robert W. Walsh https://orcid.org/0000-0002-1025-9863
Crisel Suarez https://orcid.org/0000-0001-5243-7659
Christopher S. Moore https://orcid.org/0000-0002-4103-6101
Adam R. Kobelski https://orcid.org/0000-0002-4691-1729
Jeffrey W. Reep https://orcid.org/0000-0003-4739-1152
Charles Kankelborg https://orcid.org/0000-0002-1992-7469

References

Aulanier, G., Démoulin, P., Schrijver, C. J., et al. 2013, A&A, 549, A66
Benz, A. O. 2017, LRSP, 14, 2

Boerner, P., Edwards, C., Lemen, J., et al. 2012, SoPh, 275, 41
Carmichael, H. 1964, NASSP, 50, 451
Cheung, M. C. M., Boerner, P., Schrijver, C. J., et al. 2015, ApJ, 807, 143
Czaykowska, A., Alexander, D., & De Pontieu, B. 2001, ApJ, 552, 849
Czaykowska, A., De Pontieu, B., Alexander, D., & Rank, G. 1999, ApJL, 521, L75
Del Zanna, G., Mitra-Kraev, U., Bradshaw, S. J., Mason, H. E., & Asai, A. 2011, A&A, 526, A1
Dudík, J., Janvier, M., Aulanier, G., et al. 2014, ApJ, 784, 144
Dudík, J., Polito, V., Janvier, M., et al. 2016, ApJ, 823, 41
Emslie, A. G., Dennis, B. R., Holman, G. D., & Hudson, H. S. 2005, JGRA, 110, 11103
Emslie, A. G., Dennis, B. R., Shih, A. Y., et al. 2012, ApJ, 759, 71
Fletcher, L., Dennis, B. R., Hudson, H. S., et al. 2011, SSRv, 159, 19
Graham, D. R., & Cauzzi, G. 2015, ApJL, 807, L22
Graham, D. R., Hannah, I. G., Fletcher, L., & Milligan, R. O. 2013, ApJ, 767, 83
Hansteen, V., Ortiz, A., Archontis, V., et al. 2019, A&A, 626, A33
Hinode Review Team, Al-Janabi, K., Antolin, P., et al. 2019, PASJ, 71, R1
Hirayama, T. 1974, SoPh, 34, 323
Janvier, M., Aulanier, G., Pariat, E., & Démoulin, P. 2013, A&A, 555, A77
Janvier, M., Savcheva, A., Pariat, E., et al. 2016, A&A, 591, A141
Joshi, B., Veronig, A. M., Lee, J., et al. 2011, ApJ, 743, 195
Kennedy, M. B., Milligan, R. O., Mathioudakis, M., & Keenan, F. P. 2013, ApJ, 779, 84
Kobayashi, K., Cirtain, J., Winebarger, A. R., et al. 2014, SoPh, 289, 4393
Kopp, R. A., & Pneuman, G. W. 1976, SoPh, 50, 85
Kuhar, M., Krucker, S., Hannah, I. G., et al. 2017, ApJ, 835, 6
Lemen, J. R., Title, A. M., Akin, D. J., et al. 2012, SoPh, 275, 17
Li, T., & Zhang, J. 2015, ApJL, 804, L8
Lin, R. P., Schwartz, R. A., Kane, S. R., Pelling, R. M., & Hurley, K. C. 1984, ApJ, 283, 421
Lörinčík, J., Aulanier, G., Dudík, J., Zemanová, A., & Dzifčáková, E. 2019, ApJ, 881, 68
Lörinčík, J., Polito, V., Kerr, G. S., Hayes, L. A., & Russell, A. J. B. 2025, ApJ, 986, 73
MacCombie, W. J., & Rust, D. M. 1979, SoPh, 61, 69
Masson, S., Pariat, E., Aulanier, G., & Schrijver, C. J. 2009, ApJ, 700, 559
Masuda, S., Kosugi, T., Hara, H., Tsuneta, S., & Ogawara, Y. 1994, Natur, 371, 495
Milligan, R. O., & Dennis, B. R. 2009, ApJ, 699, 968
Moore, C. S., Hong, J. S., Ho, J., et al. 2024, SPIE, 13093, 1309372
Moore, R., McKenzie, D. L., & Svestka, Z. 1980, in Solar Flares: A Monograph from Skylab Solar Workshop II, ed. P. A. Sturrock (Colorado Associated Univ. Press), 341
Moore, R. L., Sterling, A. C., Hudson, H. S., & Lemen, J. R. 2001, ApJ, 552, 833
Nakariakov, V. M., & Melnikov, V. F. 2009, SSRv, 149, 119
O'Dwyer, B., Del Zanna, G., Mason, H. E., Weber, M. A., & Tripathi, D. 2010, A&A, 521, A21
Panesar, N. K., Sterling, A. C., Moore, R. L., et al. 2018, ApJL, 868, L27
Panesar, N. K., Sterling, A. C., Moore, R. L., et al. 2019, ApJL, 887, L8
Pesnell, W. D., Thompson, B. J., & Chamberlin, P. C. 2012, SoPh, 275, 3
Priest, E., & Forbes, T. 2000, Magnetic Reconnection (Cambridge Univ. Press)
Qiu, J., & Fleming, R. 2025, SoPh, 300, 137
Qiu, J., Lee, J., Gary, D. E., & Wang, H. 2002, ApJ, 565, 1335
Qiu, J., Liu, W.-J., & Longcope, D. W. 2012, ApJ, 752, 124
Rachmeler, L. A., Winebarger, A. R., Savage, S. L., et al. 2019, SoPh, 294, 174
Reep, J. W., Warren, H. P., Moore, C. S., Suarez, C., & Hayes, L. A. 2020, ApJ, 895, 30
Reeves, K. K., Freed, M. S., McKenzie, D. E., & Savage, S. L. 2017, ApJ, 836, 55
Reeves, K. K., Warren, H. P., & Forbes, T. G. 2007, ApJ, 668, 1210
Romano, P., Falco, M., Guglielmino, S. L., & Murabito, M. 2017, ApJ, 837, 173
Sakurai, T. 2022, Physi, 5, 11
Schou, J., Scherrer, P. H., Bush, R. I., et al. 2012, SoPh, 275, 229
Sharykin, I. N., & Kosovichev, A. G. 2014, ApJL, 788, L18
Shibata, K., Masuda, S., Shimojo, M., et al. 1995, ApJL, 451, L83
Singh, V., Scullion, E., Botha, G. J. J., et al. 2025, arXiv:2507.01169
Sobotka, M., Dudík, J., Denker, C., et al. 2016, A&A, 596, A1
Sturrock, P. A. 1966, Natur, 211, 695
Sun, X., Hoeksema, J. T., Liu, Y., et al. 2013, ApJ, 778, 139
Thoen Faber, J., Joshi, R., Rouppe van der Voort, L., et al. 2025, A&A, 693, A8
Tiwari, S. K., Alexander, C. E., Winebarger, A. R., & Moore, R. L. 2014, ApJL, 795, L24
Tiwari, S. K., Hansteen, V. H., De Pontieu, B., Panesar, N. K., & Berghmans, D. 2022, ApJ, 929, 103
Tiwari, S. K., Panesar, N. K., Moore, R. L., et al. 2019, ApJ, 887, 56
Tiwari, S. K., Venkatakrishnan, P., Gosain, S., & Joshi, J. 2009, ApJ, 700, 199
Toriumi, S., Schrijver, C. J., Harra, L. K., et al. 2017, ApJ, 836, 63
Unverferth, J., & Reep, J. W. 2023, ApJ, 951, 95
Wang, Y. M. 2016, ApJL, 820, L13
Warren, H. P. 2006, ApJ, 637, 522
Warren, H. P., & Warshall, A. D. 2001, ApJL, 560, L87
Yadav, R., Kazachenko, M. D., Cauzzi, G., et al. 2025, ApJ, 989, 183
Yokoyama, T., & Shibata, K. 2001, ApJ, 549, 1160
Young, P. R. 2024, ApJ, 966, 102
Young, P. R., Doschek, G. A., Warren, H. P., & Hara, H. 2013, ApJ, 766, 127
Zweibel, E. G., & Yamada, M. 2009, ARA&A, 47, 291